Geophysical Research Letters

RESEARCH LETTER
10.1029/2021GL092714

Role of Intense Arctic Storm in Accelerating Summer Sea Ice Melt: An In Situ Observational Study

Liran Peng[1], Xiangdong Zhang[1], Joo-Hong Kim[2], Kyoung-Ho Cho[2], Baek-Min Kim[3], Zhaomin Wang[4,5], and Han Tang[1]

[1]International Arctic Research Center and Department of Atmospheric Sciences, University of Alaska Fairbanks, Fairbanks, AK, USA, [2]Korea Polar Research Institute, Incheon, South Korea, [3]Department of Environmental Atmospheric Sciences, Pukyong National University, Busan, South Korea, [4]College of Oceanography, Hohai University, Nanjing, China, [5]Southern Marine Science and Engineering Guangdong Laboratory (Zhuhai), Zhuhai, China

Abstract Intense storms have been more frequently observed in the Arctic during recent years, in coincidence with extreme sea ice loss events. However, it is still not fully understood how storms drive such events due to deficient observations and modeling discrepancies. Here we address this problem by analyzing in situ observations acquired during an Arctic expedition, which uniquely captured an intense storm in summer 2016. The result shows a pronounced acceleration of sea ice loss during the storm process. Diagnostic analysis indicates a net energy loss at the ice surface, not supporting the accelerated melting. Although the open water surface gained net heat energy, it was insufficient to increase the mixed-layer temperature to the observed values. Dynamic analysis suggests that storm-driven increase in ocean mixing and upward Ekman pumping of the Pacific-origin warm water tremendously increased oceanic heat flux. The thermal advection by the Ekman pumping led to a warmed mixed layer by 0.05°C–0.12°C and, in consequence, an increased basal sea ice melt rate by 0.1–1.7 cm day^{-1}.

Plain Language Summary More numerous storms have occurred over the Arctic during recent years, potentially impacting sea ice. Few studies have investigated the role of storms in sea ice change based on field observations. Our study aims to address the problem through analyzing changes in sea ice energy budgets during a strong storm event in summer 2016 that was associated with a rapid sea ice loss. Both atmosphere and ocean observational data were collected during a research vessel expedition in the Arctic Ocean. We found that the storm resulted in an overall heat loss from the sea ice surface to the atmosphere but a strong heat gain at the sea ice bottom from the upper ocean. Storm-induced strong anticlockwise winds drove a divergence in the upper ocean, which led to a shallowed mixed layer and enhanced mixing with the sub-surface warm water, and, in turn, an acceleration of sea ice bottom melt.

Liran Peng and Xiangdong Zhang are cofirst authors.

Key Points:

- An intense storm occurred in summer 2016 and accelerated sea ice melt in the Chukchi Sea
- A net heat energy loss occurred at sea ice surface, not supporting the accelerated sea ice melt rate
- Storm-induced increase in surface ocean mixing and upward heat transport enhanced oceanic heat flux and sea ice bottom melt

Supporting Information:

Supporting Information may be found in the online version of this article.

Correspondence to:

X. Zhang and J.-H. Kim,
xzhang9@alaska.edu;
joo-hong.kim@kopri.re.kr

Citation:

Peng, L., Zhang, X., Kim, J.-H., Cho, K.-H., Kim, B.-M., Wang, Z., & Tang, H. (2021). Role of intense Arctic storm in accelerating summer sea ice melt: An in situ observational study. *Geophysical Research Letters*, *48*, e2021GL092714. https://doi.org/10.1029/2021GL092714

Received 26 JAN 2021
Accepted 22 MAR 2021

1. Introduction

Synoptic-scale storms play important roles in modulating turbulent heat, moisture, and momentum exchanges between the atmosphere, sea ice, and ocean, and driving transient energy and water transport (e.g., Hoskins & Hodges, 2002; X. Zhang et al., 2004; X. Zhang et al., 2013; Vihma et al., 2016; Villamil-Otero et al., 2018). Studies have suggested a poleward shift of storm tracks and intensification of Arctic storm activities, though the changes in different storm characteristics are regionally and seasonally dependent (e.g., X. Zhang et al., 2004; Yin, 2005; Serreze & Barrett, 2008; Simmonds et al., 2008). Superimposed on the long-term changes, intense storms have been more frequently observed in the Arctic Ocean during recent years (Inoue et al., 2011; Simmonds & Rudeva, 2012; Aizawa & Tanaka, 2016; Tao, Zhang, Fu, & Zhang, 2017; Tao, Zhang, & Zhang, 2017). These storms may enhance atmosphere-ice-ocean interactions and cumulatively contribute to accelerating Arctic climate change (Kim et al., 2017; Moore, 2016; Rinke et al., 2017; Semenov et al., 2019).

A number of studies have examined impacts of individual storms or integrated storm activities on various aspects of Arctic sea ice and ocean properties (e.g., Yang et al., 2001, 2004; X. Zhang et al., 2004; Pickart et al., 2009; J. Zhang et al., 2013; Kriegsmann & Brümmer, 2014; Wei et al., 2019; Semenov et al., 2019). Along with the recently amplified Arctic warming (e.g., Huang et al., 2017), drastically thinning ice has become vulnerable to synoptic scale storms (e.g., Simmonds & Keay, 2009). The occurrence of the superstorm

in August 2012 and the record low sea ice extent in the following month inspired new interest in the question about how individual intense storms influence sea ice physical processes, which, in turn, cause sea ice loss (e.g., Parkinson & Comiso, 2013; J. Zhang et al., 2013).

Despite this renewed interest, studies on the topic have been few and realistic measurements of storm impacts have been hindered by the lack of in -situ observations in the Arctic Ocean. Another intense storm occurred in the summer 2016 and was followed by the third lowest minimum sea ice extent on record. Intense storms also consecutively entered the Arctic Ocean during the winters of 2015/2016 and 2016/2017, causing record warming events (Kim et al., 2017; Moore, 2016; Rinke et al., 2017), impacting surface energy budgets and, in turn, the underlying sea ice growth/melt. Fortunately, the Ice-Breaking Research Vessel (IBRV) *Araon* expedition captured the Arctic cyclone in August 2016. This provided a unique opportunity to analyze in situ observations within an active storm and gain a better understanding of the air-ice-ocean interactions that affect sea ice melt.

2. Data and Methodology

The in situ observations were acquired during the IBRV *Araon* expedition in the Chukchi and East Siberian seas from 5 to 21 August 2016. The atmospheric parameters collected included temperature, humidity, pressure, downward shortwave and longwave radiative fluxes, and wind. The wind was measured at the 33 m, which was then converted to the standard 10 m height in this study. Visible sky images were taken by an all-sky camera at 15-min intervals to provide cloud information. The sea ice surface temperatures and velocities were obtained from the ice mass balance buoy deployed approximately at (78°N, 177°W) during August 14–15, 2016. Ocean temperature, salinity, and pressure were observed using a Seabird 911 plus Conductivity-Temperature-Depth (CTD) instrument. We applied an empirical correction to the temperature and salinity profiles using the previous years' CTD measurements in the same area (the plus signs in Figure S1) to minimize the influence of slightly different locations of the CTD deployments (Text S1). With the available observations, we estimated the unobserved components of surface energy budgets (Text S2). Ocean currents measured at the CTD locations by a Lowered Acoustic Doppler Current Profiler (LADCP, RDI, 300 kHz) were used to diagnose Ekman transport based on the method in Cole et al. (2017; Text S3).

We also used the fifth generation of the European Center for Medium-Range Weather Forecasts (ECMWF) atmospheric reanalysis hourly data at a spatial resolution of 31 km (ERA5; Hersbach et al., 2020). The variables include sea level pressure (SLP), 850 hPa geopotential height, 2 m and 850 hPa temperature, net surface shortwave and net longwave radiative fluxes, and sensible and latent heat fluxes. The SLP data were used to detect the intense storm with a storm identification and tracking algorithm (X. Zhang et al., 2004). The daily Bootstrap sea ice concentration (SIC) at a spatial resolution of about 25 km (Comiso, 2017) was used to analyze the overall variation of sea ice extent. An additional SIC data product at a higher resolution of 6.25 km (Spreen et al., 2008) was employed to detect finer-scale changes of sea ice during the storm process. The polar pathfinder daily 25 km EAST-grid sea ice motion vectors (version 3) were also used for evaluating possible sea ice dynamic influence (Tschudi et al., 2016).

3. Synoptic Analysis of the Storm

The intense storm originated from the Barents Sea (Figures 1a–1f). At 00 UTC on August 13, 2016, a weak low-pressure center emerged near Novaya Zemlya, and a prior storm with moderate intensity existed over the central Arctic Ocean. The low-pressure quickly intensified when moving eastward through the Eurasian shelf seas and finally northeastward into the central Arctic Ocean. During this process, a merging with the existing storm in the central Arctic Ocean considerably contributed to its intensification. At 00 UTC on August 16, the storm developed to its mature phase with a central surface pressure of 967 hPa. Afterward, the storm entered the weakening phase. Meanwhile, another low-pressure center that underwent cyclogenesis in the Chukchi Sea coast traveled northeastward and merged with the intense storm, which sustained the storm's intensity over an extended period. A brief examination of the storm development indicates that, during the merging and resultant restrengthening processes, the baroclinic instability associated with the surface thermal contrast and an amplified upper-level Rossby wave extending into the Arctic is responsible

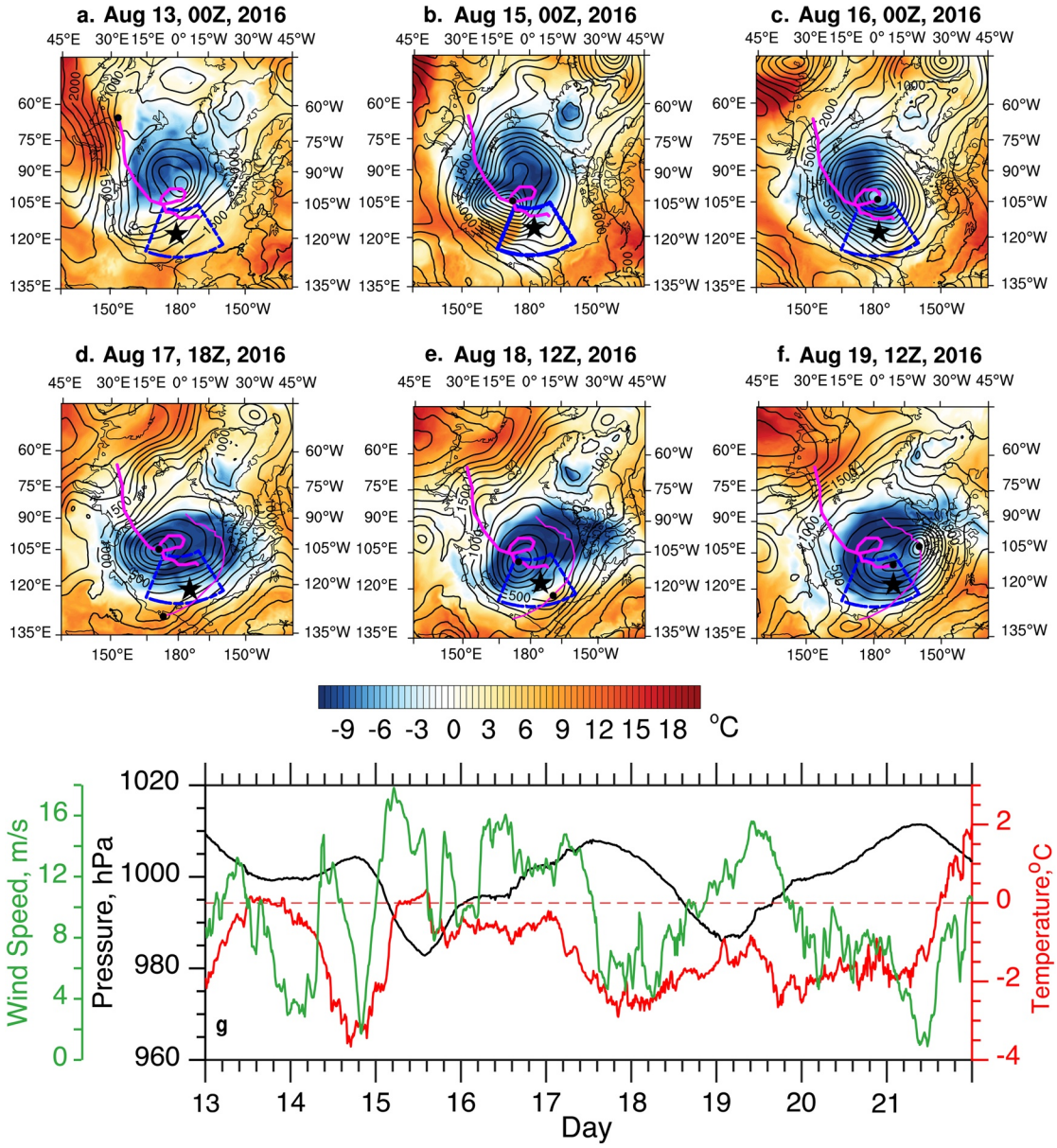

Figure 1. Geopotential height (black contours) and air temperature (color shading) at 850 hPa (a–f) using ERA5. The magenta line shows the storm track. The black dot along the track displays the storm centers. The thin magenta line shows the track of the low-pressure born in the Chukchi Sea. The black star indicates *Araon's* locations. The blue dash line highlights the study domain. (g) The time series of the surface pressure (black line), temperature (red line), and wind speed (green line) observed onboard *Araon*.

for the intensification of the storm in the early phase. The downward intrusion of the stratospheric vortex with its resulting warm core near the tropopause further intensified the storm and played primary driving role in the storm persistence, which enhanced positive vorticity advection and upper-level divergence. These specific structures and mechanisms are consistent in the findings of the existing Arctic cyclone studies (e.g., Simmonds & Rudeva, 2012; Aizawa & Tanaka, 2016; Tao, Zhang, Fu, & Zhang, 2017; Tao, Zhang, & Zhang, 2017; Yamagami et al., 2017).

The surface observations onboard *Araon* in the Chukchi Sea (star symbol in Figure 1) captured the surface pressure decrease with a minimum of 983 hPa on August 15, when the storm approached the ship and developed into its mature phase (Figure 1g). The ship observations then showed a weakening of the storm after 16 August. During August 18–19, the surface pressure decreased again to reach its second low value

when the storm merged with a new low-pressure system coming from and generated in the Chukchi Sea. The observed temperature demonstrated a large decrease from 14 to 15 August due to cold air advection when the storm became closer to *Araon* and intensified, and a follow-up increase and fluctuations due to a time-varying intrusion of warm air to the north associated with the time evolution of the storm and the merging process with the low-pressure from the Chukchi Sea.

4. Accelerated Sea Ice Decrease Associated With the Storm

To examine sea ice changes associated with the storm, we defined a study domain from 72°N to 82°N and from 158°E to 148^{o}W (the blue-dashed box in Figure 1). This domain was defined to be large enough to cover a relatively complete section of pack ice and small enough to be approximately represented by the in situ observations. The SICs and sea ice area (SIA) within the domain show an obvious decrease throughout the storm's lifetime (Figures 2a–2f). A considerably large SIC decrease occurred along the western edge since August 16, while the eastern edge only shows a slight westward retreat. Another large decrease appeared around the two open leads within the pack ice.

For a better understanding of the total sea ice changes, we constructed daily SIA anomalies in August for each year from 2010 to 2016, relative to the multiyear-mean daily SIA during the same period. We then used the SIA on 1 August to standardize the anomaly time series to reveal SIA changes with the minimized influence of different initial conditions by years. A comparison of the SIA anomalies indicates that changes in SIAs in August 2012 and 2016 drastically departed from the multiyear-mean track after the first five days, leading to the negative anomalies lower than the 25th percentile of multiyear-mean distribution (Figure 2g). Especially, the sea ice anomalies in 2012 reached the minimum value on each day among the range of sea ice anomalies from 2010–2016 all the way throughout the end of August. Note that a superstorm occurred during August 2–14 of 2012 (Simmonds & Rudeva, 2012), which was obviously responsible for the large negative SIA anomalies and could contribute to the record low SIA in September, though continuing studies are needed to reach an agreement (Parkinson & Comiso, 2013; J. Zhang et al., 2013).

The trajectory of SIA decrease in August 2016 was similar to that in August 2012 though the magnitude of the anomalies was smaller with the exception of the last five days of the study period. The decreasing rate was larger than its multiyear-mean value during August 13–22 but considerably accelerated during August 14–17 along with the storm intensification (Figure 2h). The maximum SIA decreasing rate was about 5.7 times larger than the multiyear-mean rate of 0.016 km^2 day^{-1} on August 16 when the storm reached its strongest phase. As a consequence, the SIA decreases in the study domain disproportionally contributed to about 43% of total SIA decrease in the entire Arctic Ocean, though the SIA in the study domain accounted for only about 14% of the total SIA.

5. Energy Budgets Analysis for Accelerated Sea Ice Decrease

To examine mechanisms for the accelerated SIA decrease, we quantitatively analyzed the energy budgets over the study domain. Although the westerly winds associated with the storm blew over the study domain, the pack ice was persistently limited within this domain and did not exhibit evident movement as a whole (Figure 2). The major changes in sea ice were characterized by the western and eastern ice edges shrinking toward the center of the pack ice and the enlarged opening within the pack ice. The sea ice dynamic effects mainly became an internal process within the study domain. The enhanced day-by-day, overall decrease in SIC for the whole pack ice, in particular after the drastic storm intensification, may also suggest that thermodynamically forced sea ice decrease dominated in the study domain, even if there were dynamically forced sea ice changes (e.g., deformation and fragmentation) within the domain that may enhance or weaken thermodynamic processes. To further confirm this, we employed sea ice motion and sea ice concentration dataset to calculate the sea ice area outflow across the boundaries of the study domain. We found that the mean sea ice area outflow rate (−4,274.2 km^2 day^{-1}) is only about 14.4% of the domain-mean sea ice area decreasing rate (−29,785.3 km^2 day^{-1}). We, therefore, focused on the sea ice energy budget analysis here.

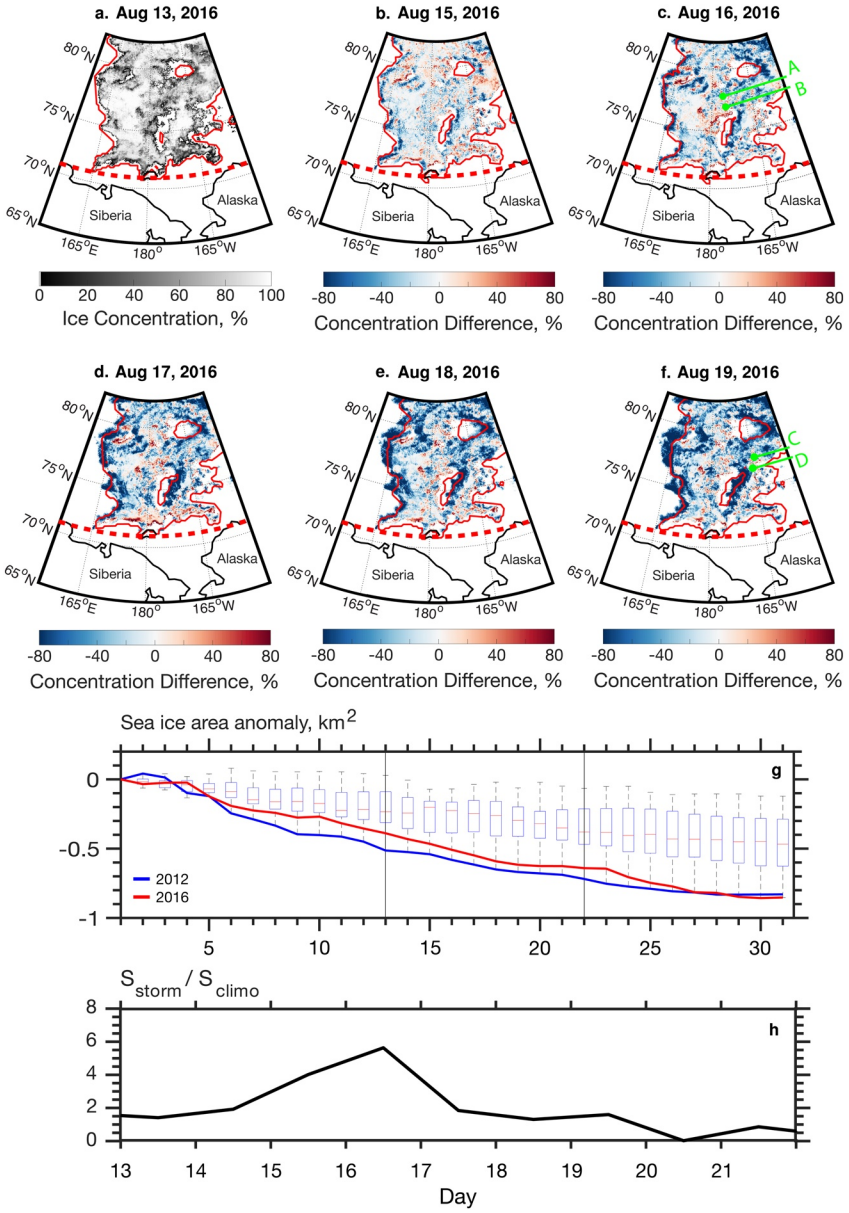

Figure 2. (a) Sea ice concentration (SIC) on August 13. The differences of SIC from (a) on (b) August 14, (c) August 16, (d) August 17, (e) August 18, and (f) August 19. The high-resolution SIC data display spatial distribution in gray in (a) and in color in (b)–(f). The Bootstrap SIC data show the ice edge in red. The thick dashed red line marks the southern boundary of the study domain. The selected CTD deployment locations on August 16 and 19 are respectively marked with A and B in (c) and C and D in (f). (g) The boxplot (showing the median, first and third quartiles, and maximum and minimum) of sea ice area (SIA) anomalies in August from 2010 to 2016, which is superimposed by the time series of the anomalies in August of 2012 (blue) and 2016 (red). (h) The ratio of SIA decreasing rate from 13 to 21 August between 2016 and the time-mean during 2010–2016.

The net surface shortwave radiative flux F_{SW} (positive downward; weighted by sea ice and open water areas (e.g., Zhang & Zhang, 2001); the same for the net surface longwave radiative flux F_{LW}, sensible heat flux F_S and latent heat flux F_L) dominated throughout the study period (Figure 3a). It ranged from about 40 W m^{-2} to 120 W m^{-2}, considerably larger than other energy flux terms. F_{SW} became generally smaller during August 13–19 when the storm influenced the study domain. In particular, F_{SW} reached a minimum on August 15 along with the drastic storm intensification. Further analysis indicated that F_{SW} decrease was mainly caused by the reduced downward shortwave radiation. Images from the upward-looking sky camera show

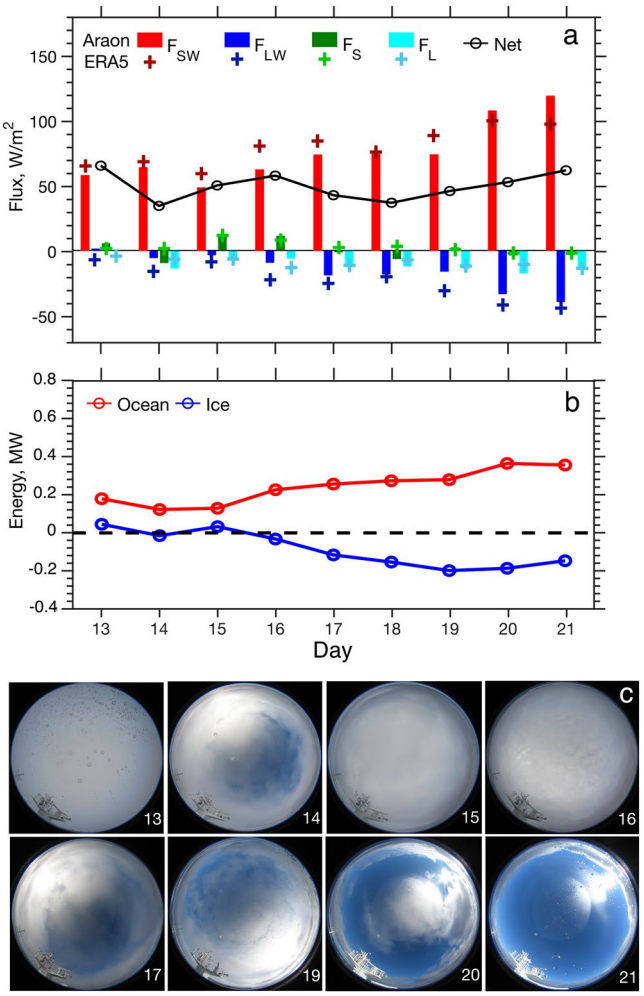

Figure 3. (a) Daily averaged net surface shortwave radiative flux (F_{SW}), net longwave radiative flux (F_{LW}), sensible heat flux (F_S), latent heat flux (F_L), and net total surface flux for the blended sea ice and open water surface. The plus signs show the daily- and domain-averaged fluxes using ERA5. (b) Net total energy into the open water (red) and sea ice (blue) surfaces. (c) All-sky camera images showing cloud conditions. The numbers at the bottom-right corner indicate the days in August 2016. The image on August 18 is not shown because its similarity to those on August.

that the reduced downward shortwave radiation was due to an increase in cloud cover (Figure 3c). F_{SW} largely increased following the storm dissipation as the clear sky prevailed after August 19. The decrease in SIC also contributed to the F_{SW} increase due to decreased surface albedo and upward shortwave radiation.

F_{LW}, $F_{S,}$ and F_L were generally negative, except the small positive values of F_S on August 15 and 16 when storm-generated warm air advection occurred in the study area. Since August 17, F_{LW} and F_L showed an increase in magnitude with time, though F_S was smaller. The increasing heat loss with time can be attributed to a combination of several contributing factors. One is the warmer sea ice surface temperature compared to the air temperature. The air temperatures generally dropped down to about −2.0°C at the observation site during August 17–21 (Figure 1g); whereas, the ice mass balance buoy observed an average temperature of −0.55°C over the same period. Also, the near-surface ocean temperature measured by CTD was around −1.2°C. The differences between sea ice/ocean and air increased vertical gradients of temperature and humidity as well as decreased near-surface boundary layer stability, leading to an increased upward turbulent heat flux. The vertical temperature differences were also manifested by the decreased downward longwave radiation measured onboard *Araon*.

As a result, the net total surface heat flux demonstrated positive values, predominantly determined by the net shortwave radiation, with an obvious decrease during the August 13–14 period when the storm intensified. The two minimum values on August 14 and 18 were ascribed to relatively large heat loss by the combined negative net longwave radiation and turbulent heat fluxes due to cold surface air temperatures and decreased cloudiness (Figures 1g and 3c). In addition, we have also analyzed the domain-averaged energy budgets from ERA5, which show good agreement with the results above (Figure 3a). This demonstrates the robustness of the energy budget analysis using the in situ observations and its representation of the study domain.

The conventional energy budget analysis above for the blended sea ice and open water surfaces indicates an overall surface energy gain. However, further analysis on the partitioning of the total heat energy into the sea ice and open water surfaces separately shows a large heat loss from the sea ice surface despite a slight heat gain on August 13 and 15 (Figure 3b). The largest heat loss at sea ice surface occurred on August 19 when the combined negative F_{LW} and F_L became relatively large, but the positive F_{SW} had not greatly increased due to cloud cover. This suggests that changes in the sea ice surface heat budgets did not contribute to the observed acceleration of sea ice decrease during storm passage (Figure 2). Nevertheless, the open water surface in the domain gained heat due to the increased net total heat flux (Figure 3a) and decreased SIC (Figure 2), which may have contributed to an increase in mixed layer ocean temperature and heat content and, in turn, basal sea ice melt.

To understand the role of ocean temperature change in sea ice bottom melt, we estimated oceanic heat flux F_{io}, (i.e., turbulent heat flux from the ocean to the bottom of sea ice; McPhee, 1992) using CTD measurements. The CTD was deployed from the *Araon*. We selected two groups of the available CTD measurements (Group 1: A and B in Figure 2c; Group 2: C and D in Figure 2f) for estimating F_{io}. The result shows an increase in surface mixed layer (SML) temperature (an average above 20 m, seeing discussions in the next section) by 0.05°C (0.05°C above salinity-dependent freezing points) from 06 UTC to 19 UTC on 16 August and 0.12°C (0.11°C above salinity-dependent freezing pints) from 02 UTC to 11 UTC on 19 August (A vs. B and C vs. D) (SI Table S1). Correspondingly, F_{io} largely increased from 98.5 ± 37.2 W m^{-2} at 06 UTC to

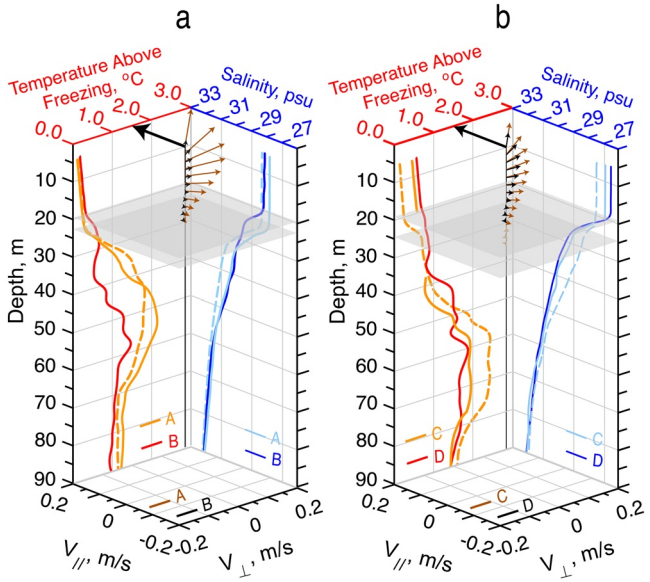

Figure 4. (a) Profiles of the temperature-above-freezing-point and salinity from the CTDs and the diagnosed corresponding Ekman transport and mixed layer depths at 06 UTC and 19 UTC (denoted by A and B) on August 16, 2016. (b) The same as (a) but for 02 UTC and 11 UTC (denoted by C and D) on August 19, 2016. The locations of A-D are shown in Figure 2. The dashed lines show the original profiles at A and (c) The solid orange and light blue lines represent the corrected profiles at A and C relative to B and D shown by the solid red and blue lines. The thick black arrow at the surface indicates the surface ocean velocity, and the thin black and brown arrows at each vertical level represent the Ekman velocity with scales shown at the bottom of (a) and (b). The gray shaded planes represent the mixed layer depths.

102.1 ± 38.6 W m^{-2} 19 UTC on August 16 and 148.1 ± 56.1 W m^{-2} at 02 UTC to 206.0 ± 78.1 Wm^{-2} at 11 UTC on 19 August. During the summer season, conductive heat flux is negligible and F_{io} is predominantly used for sea ice bottom melt. Following Steele and Ermold (2015), the sea ice bottom melt rate was estimated to increase from 2.83 ± 1.07 cm day^{-1} to 2.93 ± 1.11 cm day^{-1} on August 16 and from 4.25 ± 1.61 cm day^{-1} to 5.91 ± 2.24 cm day^{-1} on August 19. Consequently, the sea ice melt in the study domain could be solely attributed to the increased oceanic heat flux considering the net heat energy loss at the sea ice surface.

Now, another question emerges: Is the absorbed heat energy by the open water surface from the atmosphere the only source for the SML warming? To answer this question, we estimated the possible SML temperature changes caused by the net energy input from the open water surface for the two periods corresponding to the deployment times in each of the two CTD groups. We found an increase of 0.0076°C on 16 August and 0.0063°C on August 19 in SML temperature, which is much smaller than the changes in the CTD measured SML temperatures (Table S1). Therefore, we need to identify other sources in the ocean, which we hypothesized would be from changing ocean dynamics driven by the storm.

6. Role of Storm-Forced Changes in Ocean Dynamics

To identify heat source in the ocean and examine its role in increasing SML temperature and accelerating sea ice melt, we analyzed the vertical profiles of temperature and salinity measured by the two groups of CTDs. We also conducted a diagnostic analysis of mixed layer depth and Ekman dynamics associated with the winds observed onboard *Araon* (Text S3).

The temperature and salinity profiles show nearly constant from the surface down to 20–25 m (Figure 4). This depth is consistent with the diagnosed mixed layer depth, which is defined as the level where the potential density relative to 0 dbar exceeds its value at the shallowest level by 0.1 kg m^{-3} (e.g., Toole et al., 2010). This suggests a dynamic role of the storm in the upper ocean mixing process. The storm drastically intensified from 15-16 August, and the observed in situ wind speed increased accordingly (Figure 1). The stronger wind generated deeper mixed layer depth than the multiyear composite means and previous climatological estimates in the region (e.g., Peralta-Ferriz & Woodgate, 2015). The small decrease in the mixed layer depth from 06 UTC to 19 UTC on August 16 could be attributed to the slight weakening of winds (Figure 1g). Restratification from the increased basal sea ice melt might also have a contribution. Similarly, a deeper mixed layer depth also occurred on 19 August along with the largely increased wind speed during the same period when the storm reenergized due to the merging process with a new low pressure originating from the Chukchi Sea as discussed above (Figure 1). Nevertheless, the mixed layer depth also showed a decrease from 02 UTC to 11 UTC, which can be explained by the changes in the salinity profile below.

Consistent warming of SML occurred on both 16 and 19 August. In contrast, the maximum warm temperatures from 30 to 70 m in Group 1 and 50–80 m in Group 2 largely decreased, indicating a large cooling of the Pacific-origin warm water. Meanwhile, an increase in temperature occurred in the layer just beneath SML and above the Pacific-origin warm water layer from 20 to 30 m in Group 1 and 40–50 m in Group 2. These can be ascribed to the storm-induced changes in ocean dynamics. According to Figure 4, the diagnosed Ekman transport shows a clockwise spiral vertically. Considering that the CTDs were deployed to the south of the storm center, the Ekman transport diverged ocean water within the Ekman layer from the northern Chukchi-Beaufort seas, but simultaneously caused convergences underneath. The resulting Ekman pumping led to vertical heat transport into SML and an elevation of the Pacific warm water layer, weakening

the original Pacific warm water layer. A further analysis of surface wind stress curl using the ERA5 data suggests a dominant upward motion in the study domain (Figure S2). This supports the theoretical analysis here based on the ship observation. The larger wind speed resulted in a deeper mixed layer depth and a shallower Pacific water layer on August 19 compared with that on August 16. During this process, enhanced mixing would have occurred across different water mass between the SML, halocline, and Pacific warm water, leading to a deeper and well-mixed SML.

Also, the Ekman transport was in the opposite direction to the climatologically westward to northwestward currents along the shelf break, reducing the Pacific-origin warm water inflow into the study domain. This would further suggest that the combined impacts of the upward Ekman pumping and enhanced SML mixing (including entraining process with diapycnal mixing) largely contributed to the observed SML warming.

Accompanying the SML warming, slight salinization occurred in Group 1 on August 16. This could also be attributed to the upward Ekman transport of and mixing with the underneath saltier Pacific-origin water when the sea ice melting water had not been enough to dominate the SML. However, the accelerated sea ice melt on August 19 diluted the saltier water by the Ekman pumping, leading to a freshening SML (Figure 4b). At the same time, the enhanced Ekman upwelling advected a larger amount of the saltier Pacific-origin water to the bottom of the SML as shown by the salinization between 50 and 20 m in the salinity profiles in Figure 4b. Taken together, a shallowing of the mixed layer depth and a strengthening of stratification of the halocline occurred as mentioned above.

7. Discussion and Summary

We employed in situ observations to quantitatively analyze changes in sea ice and underlying physical process associated with an intense storm in mid-August 2016, which was followed by the third lowest sea ice extent on record. The results indicate that sea ice melt considerably accelerated during the process of the intense storm compared with climatology for recent decades. The result of the diagnostic analysis shows a net heat energy loss at the sea ice surface, which did not support the observed acceleration of sea ice melt. Although the open water surface gained net heat energy from the overlying atmosphere, it was not sufficient to increase SML temperature to CTD observed values. The upper ocean dynamic analysis using the in situ wind observational data suggests that the storm-induced Ekman pumping enhanced upward heat transports and caused the elevation of the Pacific-origin warm water layer. The wind stress curl analysis based on the ERA5 reanalysis for the entire study domain also provides an additional support for the enhanced Ekman-pumping. During this process, although the SML lost heat to melt sea ice, the combined heat input into the SML from the open water surface and deeper ocean layer exceeded this heat loss, leading to a warmed SML, which is manifested by the increase in the SML temperature measured by CTDs. Meanwhile, the increased ocean mixing results in a well-mixed, homogenously distributed warmer temperature in the SML. These dynamically driven processes predominantly contributed to an increase in oceanic heat flux and an enhanced basal sea ice melt.

This study reveals opposite net heat energy budgets at sea ice surface and open water surfaces and suggests a leading role of dynamically-driven vertical ocean heat transport and upper ocean mixing in sea ice melt associated with an intense storm. The results and the associated in situ observations provide observational insight, facilitating evaluation and improvement of model simulations on the topic (e.g., J. Zhang et al., 2013; Semenov et al., 2019). Nevertheless, there are still existing uncertainties and open questions. In situ observations are continually deficient. This raises a grand challenge for better understanding of storm-induced changes in the Arctic system in different regions and seasons with different atmosphere, sea ice, and ocean states. More feedback processes need to be carefully examined with improved, high-resolution data and models. Especially, the observed changes in sea ice concentration include those caused by both dynamically forced opening and thermodynamically driven melt. The interactions of dynamic and thermodynamic processes in causing an overall sea ice melt have therefore been included in the heat energy budget analysis in this study. It is still interesting to further distinguish how each particular piece of sea ice is drifted to a warmer or colder area to accelerate or decelerate sea ice melt. But this needs high-resolution, spatially-well-covered data and beyond the scope of the current study, which would also be a follow-up research using a high-resolution model when available and realistic.

Data Availability Statement

The ERA5 data were obtained from the Copernicus Climate Change Service (C3S) Climate Data Store (https://cds.climate.copernicus.eu/) and the satellite sea ice concentration data were from the NSIDC (https://nsidc.org/). The *Araon* observations are available at the Korea Polar Data Center (https://kpdc.kopri.re.kr) with the data DOIs https://dx.doi.org/doi:10.22663/KOPRI-KPDC-00001456.1 for the CTD data, https://dx.doi.org/doi:10.22663/KOPRI-KPDC-00001637.1 for the meteorological data, https://dx.doi.org/doi:10.22663/KOPRI-KPDC-00001458.1 for the sea ice buoy data, and https://dx.doi.org/doi:10.22663/KOPRI-KPDC-00001634.1 for the LADCP data at the four CTD deployment sites.

Acknowledgments
This study was supported by DOE grant DE-SC0020640, NSF grant ARC-1023592, and KOPRI projects KPOPS-Earth (KOPRI, PE21010) and K-AOOS (20160245, funded by the MOF, Korea). Zhaomin Wang was supported by the National Natural Science Foundation of China Grant 41941007 and 41876220. We thank the editor Dr. Andy Hogg, two anonymous reviewers, and the reviewer Dr. Wenli Zhong for their constructive reviews, which helped improve the content and presentation of this paper. The ice mass balance buoy was deployed with J. P. Wilkinson as part of the collaboration of K-AOOS with ICE-ARC-EU FP7 project. Zhelin Xie participated in the field observations.

References

Aizawa, T., & Tanaka, H. L. (2016). Axisymmetric structure of the long lasting summer Arctic cyclones. *Polar Science*, *10*, 192–198. https://doi.org/10.1016/j.polar.2016.02.002

Cole, S. T., Toole, J. M., Lele, R., Timmermans, M.-L., Gallaher, S. G., Stanton, T. P., et al. (2017). Ice and ocean velocity in the Arctic marginal ice zone: Ice roughness and momentum transfer. *Elementa Science of the Anthropocene*, *5*, 55. https://doi.org/10.1525/elementa.241

Comiso, J. C. (2017). *Bootstrap sea ice concentrations from Nimbus-7 SMMR and DMSP SSM/I-SSMIS, version 3. (Indicate subset used)*. NASA National Snow and Ice Data Center Distributed Active Archive Center. https://doi.org/10.5067/7Q8HCCWS4I0R

Hersbach, H., Bell, B., Berrisford, P., Hirahara, S., Horányi, A., Muñoz-Sabater, J., et al. (2020). The ERA5 global reanalysis. *Quarterly Journal of the Royal Meteorological Society*, *146*, 1999–2049. https://doi.org/10.1002/qj.3803

Hoskins, B. J., & Hodges, K. I. (2002). New perspectives on the Northern Hemisphere winter storm tracks. *Journal of the Atmospheric Sciences*, *59*, 1041–1061. https://doi.org/10.1175/1520-0469(2002)059<1041:npotnh>2.0.co;2

Huang, J., Zhang, X., Zhang, Q., Lin, Y., Hao, M., Luo, Y., et al. (2017). Recently amplified arctic warming has contributed to a continual global warming trend. *Nature Climate Change*, *7*, 875–879. https://doi.org/10.1038/s41558-017-0009-5

Inoue, J., & Hori, M. E. (2011). Arctic cyclogenesis at the marginal ice zone: A contributory mechanism for the temperature amplification? *Geophysical Research Letters*, *38*, L12502. https://doi.org/10.1029/2011GL047696

Kim, B.-M., Hong, J.-Y., Jun, S.-Y., Zhang, X., Kwon, H., Kim, S.-J., et al. (2017). Major cause of unprecedented Arctic warming in January 2016: Critical role of an Atlantic windstorm. *Scientific Reports*, *7*, 40051. https://doi.org/10.1038/srep40051

Kriegsmann, A., & Brümmer, B. (2014). Cyclone impact on sea ice in the central Arctic Ocean: A statistical study. *The Cryosphere*, *8*, 303–317. https://doi.org/10.5194/tc-8-303-2014

McPhee, M. G. (1992). Turbulent heat flux in the upper ocean under sea ice. *Journal of Geophysical Research*, *97*, 5365–5379. https://doi.org/10.1029/92jc00239

Moore, G. W. K. (2016). The December 2015 North Pole warming event and the increasing occurrence of such events. *Scientific Reports*, *6*, 39084. https://doi.org/10.1038/srep39084

Parkinson, C. L., & Comiso, J. C. (2013). On the 2012 record low Arctic sea ice cover: Combined impact of preconditioning and an August storm. *Geophysical Research Letters*, *40*, 1356–1361. https://doi.org/10.1002/grl.50349

Peralta-Ferriz, C., & Woodgate, R. A. (2015). Seasonal and interannual variability of pan-Arctic surface mixed layer properties from 1979 to 2012 from hydrographic data, and the dominance of stratification for multiyear mixed layer depth shoaling. *Progress in Oceanography*, *134*, 19–53. https://doi.org/10.1016/j.pocean.2014.12.005

Pickart, R. S., Moore, G. W. K., Torres, D. J., Fratantoni, P. S., Goldsmith, R. A., & Yang, J. (2009). Upwelling on the continental slope of the Alaskan Beaufort Sea: Storms, ice, and oceanographic response. *Journal of Geophysical Research*, *114*, C00A13. https://doi.org/10.1029/2008JC005009

Rinke, A., Maturilli, M., Graham, R. M., Matthes, H., Handorf, D., Cohen, L., et al. (2017). Extreme cyclone events in the Arctic: Wintertime variability and trends. *Environmental Research Letters*, *12*(9), 094006. https://doi.org/10.1088/1748-9326/aa7def

Semenov, A., Zhang, X., Rinke, A., Dorn, W., & Dethloff, K. (2019). Arctic Intense Summer Storms and Their Impacts on Sea Ice-A Regional Climate Modeling Study. *Atmosphere*, *10*(4), 218. https://doi.org/10.3390/atmos10040218

Serreze, M. C., & Barrett, A. P. (2008). The summer cyclone maximum over the Central Arctic Ocean. *Journal of Climate*, *21*, 1048–1065. https://doi.org/10.1175/2007jcli1810.1

Simmonds, I., Burke, C., & Keay, K. (2008). Arctic climate change as manifest in cyclone behavior. *Journal of Climate*, *21*, 5777–5796. https://doi.org/10.1175/2008JCLI2366.110.1175/2008jcli2366.1

Simmonds, I., & Keay, K. (2009). Extraordinary September Arctic sea ice reductions and their relationships with storm behavior over 1979-2008. *Geophysical Research Letters*, *36*, L19715. https://doi.org/10.1029/2009GL039810

Simmonds, I., & Rudeva, I. (2012). The great Arctic cyclone of August 2012. *Geophysical Research Letters*, *39*, a. https://doi.org/10.1029/2012GL054259

Spreen, G., Kaleschke, L., & Heygster, G. (2008). Sea ice remote sensing using AMSR-E 89-GHz channels. *Journal of Geophysical Research*, *113*, C02S03. https://doi.org/10.1029/2005JC003384

Steele, M., & Ermold, W. (2015). Loitering of the retreating sea ice edge in the Arctic Seas. *Journal of Geophysical Research: Oceans*, *120*, 7699–7721. https://doi.org/10.1002/2015JC011182

Tao, W., Zhang, J., Fu, Y., & Zhang, X. (2017). Driving roles of tropospheric and stratospheric thermal anomalies in intensification and persistence of the Arctic Superstorm in 2012. *Geophysical Research Letters*, *44*, 10017–10025. https://doi.org/10.1002/2017GL074778

Tao, W., Zhang, J., & Zhang, X. (2017). The role of stratosphere vortex downward intrusion in a long-lasting late-summer Arctic storm. *Quarterly Journal of the Royal Meteorological Society*, *143*, 1953–1966. https://doi.org/10.1002/qj.3055

Toole, J. M., Timmermans, M.-L., Perovich, D. K., Krishfield, R. A., Proshutinsky, A., & Richter-Menge, J. A. (2010). Influences of the ocean surface mixed layer and thermohaline stratification on Arctic Sea ice in the central Canada Basin. *Journal of Geophysical Research*, *115*, C10018. https://doi.org/10.1029/2009JC005660

Tschudi, M., Fowler, C., Maslanik, J., Stewart, J. S., & Meier, W. N. (2016). *Polar pathfinder daily 25 km EAST-grid sea ice motion vectors, version 3. Boulder, Colorado, USA. NASA National Snow and ice data center distributed active Archive center*. https://doi.org/10.5067/O57VAIT2AYYY

Vihma, T., Screen, J., Tjernström, M., Newton, B., Zhang, X., Popova, V., et al. (2016). The atmospheric role in the Arctic water cycle: A review on processes, past and future changes, and their impacts. *Journal of Geophysical Research: Biogeoscience*, *121*, 586–620. https://doi.org/10.1002/2015JG003132

Villamil-Otero, G. A., Zhang, J., He, J., & Zhang, X. (2018). Role of extratropical cyclones in the recently observed increase in poleward moisture transport into the Arctic Ocean. *Advances in Atmospheric Sciences*, *35*, 85–94. https://doi.org/10.1007/s00376-017-7116-0

Wei, J., Zhang, X., & Wang, Z. (2019). Impacts of extratropical storm tracks on Arctic sea ice export through Fram Strait. *Climate Dynamics*, *52*(3-4), 2235–2246. https://doi.org/10.1007/s00382-018-4254-8

Yamagami, A., Matsueda, M., & Tanaka, H. L. (2017). Extreme Arctic cyclone in August 2016. *Atmospheric Science Letters*, *18*, 307–314. https://doi.org/10.1002/ask.75710.1002/asl.757

Yang, J., Comiso, J., Krishfield, R., & Honjo, S. (2001). Synoptic storms and the development of the 1997 warming and freshening event in the Beaufort Sea. *Geophysical Research Letters*, *28*, 799–802. https://doi.org/10.1029/2000JC00058310.1029/2000gl011896

Yang, J., Comiso, J., Walsh, D., Krishfield, R., & Honjo, S. (2004). Storm-driven mixing and potential impact on the Arctic Ocean. *Journal of Geophysical Research*, *109*, C04008. https://doi.org/10.1029/2001JC001248

Yin, J. H. (2005). A consistent poleward shift of the storm tracks in simulations of 21st century climate. *Geophysical Research Letters*, *32*, a. https://doi.org/10.1029/2005GL023684

Zhang, J., Lindsay, R., Schweiger, A., & Steele, M. (2013). The impact of an intense summer cyclone on 2012 Arctic sea ice retreat. *Geophysical Research Letters*, *40*, 720–726. https://doi.org/10.1002/grl.50190

Zhang, X., He, J., Zhang, J., Polyakov, I., Gerdes, R., Inoue, J., & Wu, P. (2013). Enhanced poleward moisture transport and amplified northern high-latitude wetting trend. *Nature Climate Change*, *3*, 47–51. https://doi.org/10.1038/NCLIMATE1631

Zhang, X., Walsh, J. E., Zhang, J., Bhatt, U. S., & Ikeda, M. (2004). Climatology and Interannual Variability of Arctic Cyclone Activity: 1948-2002. *Journal of Climate*, *17*, 2300–2317. https://doi.org/10.1175/1520-0442(2004)017<2300:caivoa>2.0.co;2

Zhang, X., & Zhang, J. (2001). Heat and freshwater budgets and their pathways in the Arctic Mediterranean in a coupled Arctic Ocean/Sea-ice model. *Journal of Oceanography*, *57*, 207–234.

References From the Supporting Information

Cole, S. T., Timmermans, M.-L., Toole, J. M., Krishfield, R. A., & Thwaites, F. T. (2014). Ekman veering, internal waves, and turbulence observed under Arctic sea ice. *Journal of Physical Oceanography*, *44*, 1306–1328. https://doi.org/10.1175/jpo-d-12-0191.1

Ekman, V. W. (1905). On the influence of the earth's rotation on ocean currents. *Arkiv För Matematik, Astronomi Och Fysik*, *2*, 1–53.

Krishfield, R. A., & Perovich, D. K. (2005). Spatial and temporal variability of oceanic heat flux to the Arctic ice pack. *Journal of Geophysical Research*, *110*, C07021. https://doi.org/10.1029/2004JC002293

Large, W. G., & Yeager, S. (2004). *Diurnal to decadal global forcing for ocean and sea-ice models: The data sets and flux climatologies, NCAR Tech. Note: NCAR/TN-460+STR* (p. 105). CGD Division of the National Center for Atmospheric Research.

McPhee, M. G. (1999). Parameterization of mixing in the ocean boundary layer. *Journal of Marine Systems*, *21*, 55–65. https://doi.org/10.1016/S0924-7963(99)00005-6

McPhee, M. G. (2002). Turbulent stress at the ice/ocean interface and bottom surface hydraulic roughness during the SHEBA drift. *Journal of Geophysical Research*, *107*, 8037. https://doi.org/10.1029/2000JC000633

McPhee, M. G. (2008). *Air-ice-ocean interaction: Turbulent ocean boundary layer exchange processes* (p. 226). Springer.

McPhee, M. G., Kikuchi, T., Morison, J. H., & Stanton, T. P. (2003). Ocean-to-ice heat flux at the North Pole environmental observatory. *Geophysical Research Letters*, *30*, 2274. https://doi.org/10.1029/2003GL018580

Millero, F. J. (1978). Freezing point of seawater. *UNESCO Tech. Papers in Marine Science*, *28*, 35.

Nihashi, S., & Ohshima, K. I. (2008). Bulk heat transfer coefficient in the ice-upper ocean system in the ice melt season derived from concentration-temperature relationship. *Journal of Geophysical Research*, *113*, C06008. https://doi.org/10.1029/2007JC004127

Perovich, D. K., Grenfell, T. C., Light, B., & Hobbs, P. V. (2002). Seasonal evolution of the albedo of multiyear Arctic sea ice. *Journal of Geophysical Research*, *107*(C10), 8044. https://doi.org/10.1029/2000JC000438

Perovich, D. K., Nghiem, S. V., Markus, T., & Schweiger, A. (2007). Seasonal evolution and interannual variability of the local solar energy absorbed by the Arctic sea ice-ocean system. *Journal of Geophysical Research*, *112*, C03005. https://doi.org/10.1029/2006JC003558